

Characterization and Modeling of Precipitation Kinetics in a Fe-Si-Ti Alloy

MALIKA PERRIER, ALEXIS DESCHAMPS, OLIVIER BOUAZIZ, YVES BRECHET, FRÉDÉRIC DANOIX, FRÉDÉRIC DE GEUSER, PATRICIA DONNADIEU, KHALID HOUMMADA, and PHILIPPE MAUGIS

In this article, we present a systematic study of precipitation kinetics in a Fe-Si-Ti alloy in the temperature range 723 K to 853 K (450 °C to 580 °C), combining complementary tools (transmission electron microscopy (TEM), atom probe tomography (APT), and small-angle neutron scattering (SANS)). We show that the Heusler phase Fe_2SiTi dominates the precipitation process in the investigated time and temperature range, regardless of the details of the initial temperature history. A numerical model based on the evolution of precipitate size classes gives very good agreement with the experimental results, and its application to different alloy compositions provides directions for future alloy optimization.

DOI: 10.1007/s11661-012-1337-8

© The Minerals, Metals & Materials Society and ASM International 2012

I. INTRODUCTION

AMONG the precipitation hardening steels, the Fe-Si-Ti system has received some attention for nearly a century,^[1–15] particularly before the 1980s and with a more recent revival. This system is capable of forming a large volume fraction of intermetallic phases^[9,11] that can substantially increase the material's strength, with the possibility of a solution treatment in the ferritic domain, so that no allotropic phase transformation occurs during quenching from the solution treatment temperature. Given the low density of the two solute elements, this system is an attractive solution for increasing the strength of steels (*e.g.*, in automotive applications) in conjunction with substantial weight savings.

A number of phases can form in this ternary system.^[13,14,16] In addition to the main phases of the binary Fe-Si and Fe-Ti systems (Fe_3Si and Fe_2Ti), Xiong *et al.*^[14] reviewed a large number of stable and metastable phases that are susceptible to form in the ternary system.

Several authors agree that at high temperature (above 1070 K (797 °C)), the precipitation in alloys with

composition of the order of Fe-3.5 wt pct Si-1.5 wt pct Ti is dominated by the Laves phase Fe_2Ti .^[3,4,15] At lower temperatures, most authors consider that the main phase that forms is the metastable Heusler phase Fe_2SiTi .^[8–10,15] However the stability range of this phase is not clear, since it has been observed by some authors to remain for relatively long aging times and by others to be replaced by the Fe_2Ti phase progressively.

The high volume fractions that can be obtained with this phase and its very small size, associated with its coherency with the matrix, make it difficult to characterize quantitatively its precipitation kinetics by conventional means, such as transmission electron microscopy (TEM). Thus, to this day, very few kinetic studies on this system are available in the literature.^[4,11]

A full kinetic study requires the use of a combination of complementary tools.^[17] Structural information about the precipitate type can be obtained by TEM, while the chemical composition of the nanoscale precipitates can be obtained by atom probe tomography (APT). The evolution of precipitate size and volume fraction, although in principle accessible by the aforementioned techniques, is obtained with a much higher precision using small-angle neutron scattering (SANS). In this article, we will carry out a systematic study coupling these three experimental techniques to reach a thorough understanding of the kinetics of precipitate formation in the temperature range of interest for precipitation strengthening, namely, 723 K to 853 K (450 °C to 580 °C). TEM and APT will help determine the nature and composition of the phases forming along the investigated heat treatments, and SANS will provide a quantitative determination of the precipitation kinetics. In addition, the quantitative data from the SANS experiments will be compared to the outcome of a precipitation model, providing insight into the thermodynamic and kinetics parameters of precipitation in this system.

MALIKA PERRIER, formerly PhD Student with SIMAP, INP-Grenoble, St Martin d'Hères Cedex, France, is now Research Engineer with Constellium Research Centre, Voreppe, France. ALEXIS DESCHAMPS and YVES BRECHET, Professors, are with the SIMAP, INP-Grenoble, Contact e-mail: alexis.deschamps@grenoble-inp.fr OLIVIER BOUAZIZ, Research Scientist, is with the Arcelor-mittal Research SA, Maizières les Metz, France. FRÉDÉRIC DANOIX, Research Scientist, is with the GPM, CNRS, Rouen, France. FRÉDÉRIC DE GEUSER and PATRICIA DONNADIEU, Research Scientists, are with the SIMAP, CNRS, Grenoble, France. KHALID HOUMMADA, Assistant Professor, and PHILIPPE MAUGIS, Professor, are with the Aix-Marseille Université, Marseille, France.

Manuscript submitted March 30, 2012.

Article published online October 12, 2012

Table I. Composition of the Investigated Alloy

Element	Si	Ti	C	S	Mn	P	B	N
Concentration (Wt pct)	2.54	1.05	0.0072	0.0008	0.005	0.003	<0.001	0.0004

II. MATERIAL AND EXPERIMENTAL TECHNIQUES

A. Material and Heat Treatments

The composition of the investigated alloy that was cast at ArcelorMittal Research S.A. is given in Table I. Apart from the small carbon content that resulted in the formation of a small amount of TiC particles, the alloy is essentially a ternary Fe-Si-Ti alloy. The as-cast ingots were cut into 50-mm-thick slabs and hot-rolled between 1467 K and 1253 K (1194 °C and 980 °C), followed by cold rolling down to a final thickness of 0.9 mm. The alloy was then solution treated in a salt bath at 1173 K (900 °C) for 5 minutes. At this temperature, the alloy is fully ferritic and fully recrystallized with an average grain size of 20 μm . The main heat treatment route was then to quench and hold the samples in a salt bath for 10 minutes at the aging temperature (so as to ensure a rapid and reproducible heating rate) and then to transfer them into a tube furnace for further aging. In order to evaluate the possible influence of the early stage temperature history, other processing routes were investigated. A first alternative route was to increase the preaging time in the salt bath to 30 minutes. A second alternative route was to perform the entire heat treatment in a halogen furnace, where cooling from the solution treatment temperature (1173 K (900 °C)) to the aging temperature (823 K (550 °C)) was achieved at a rate of 8 °C/s. The last route (referred as “as quenched”) was to quench the sample from the solution treatment temperature into cold water and then to perform the heat treatment in the tube furnace.

B. Characterization Techniques

For TEM studies, specimens were mechanically polished down to 80 to 100 μm and then twin-jet electropolished between 289 K (16 °C) and 291 K (18 °C) in a solution of ethylene glycol monobutyl ether (90 pct) and perchloric acid (10 pct). Subsequently, the samples were cleaned for oxidation by ion milling (3 keV PIPS, 5 deg incidence angle). Observations were carried out on a JEOL*

*JEOL is a trademark of Japan Electron Optics Ltd., Tokyo.

3010 microscope operating at 300 kV.

For APT analyses, samples of dimensions 300 μm \times 300 μm \times 2 cm were cut and electropolished using the two-stage method.^[18] Experiments were carried out on a Cameca LEAP 3000HR at IM2NP (Université Paul Cézanne Aix-Marseille, Marseille, France). All analyses were in voltage mode, with a pulse fraction of 20 pct and a base temperature of 80 K. Data were processed using IVAS 3.5 software.

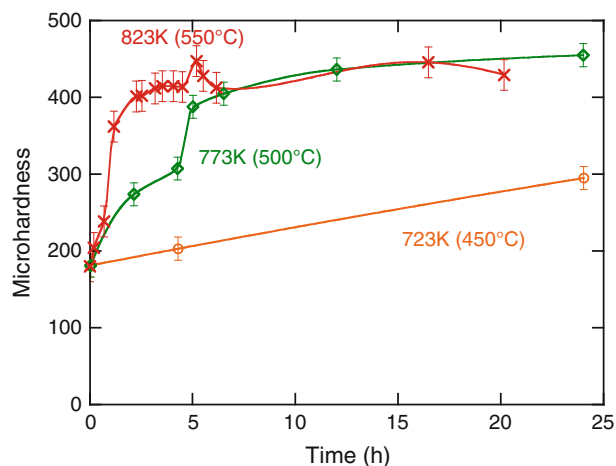


Fig. 1—Microhardness evolution during aging at 723 K, 773 K, and 823 K (450 °C, 500 °C, and 550 °C).

The small-angle neutron scattering experiments were carried out at Institut Laue Langevin (ILL, Grenoble, France) on instrument D11. The samples were kept at the initial thickness of 0.9 mm, and the measured area was 10 mm \times 10 mm. They were polished on both sides to 1- μm diamond paste. Experiments were carried out at a wavelength of 6 Å to avoid any diffraction, under a magnetic field of 1.5 T, to separate the nuclear and magnetic contributions to the contrast of neutron scattering length between the precipitates and matrix. Three sample-to-detector distances were used, namely, 2 m, 5.5 m, and 16.5 m, which resulted in a measured range of scattering vectors of [0.004 Å⁻¹, 0.22 Å⁻¹]. Data analysis was carried out using the GRASP software developed at ILL. Data were corrected from detector efficiency and background noise and were normalized to absolute values using a reference water cell.

III. EXPERIMENTAL RESULTS

A. Hardness Evolution

Figure 1 shows the microhardness evolution for three aging temperatures, namely, 723 K, 773 K, and 823 K (450 °C, 500 °C, and 550 °C). When temperature increases, the precipitation kinetics becomes faster. A strong precipitation hardening increment is found, with a maximum hardness of about 420 to more than 450 HV, depending on the aging temperature. The measured yield strength at peak hardness at 823 K (550 °C) was about 1200 MPa. In the following, the precipitation behavior was mainly studied at 823 K (550 °C). Other aging temperatures were only characterized by SANS.

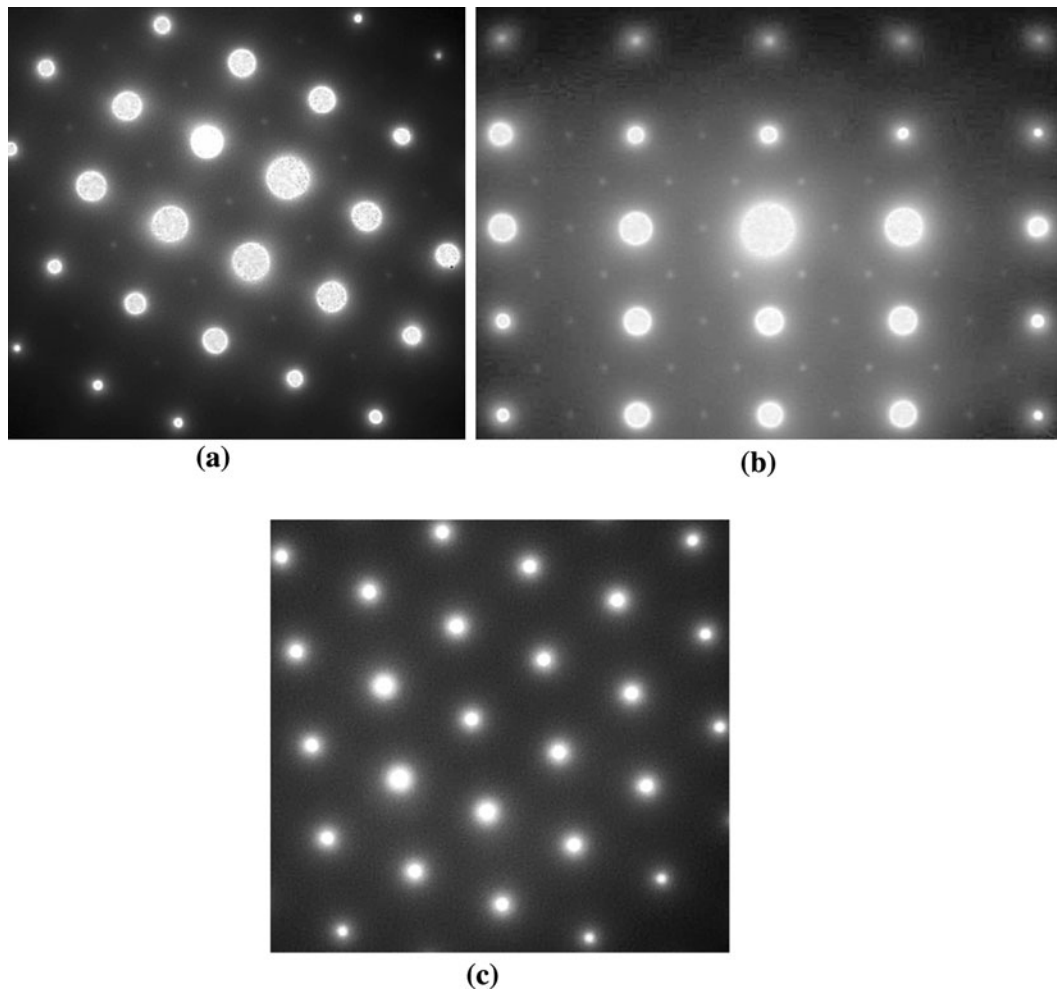


Fig. 2—Diffraction patterns of the alloy aged 3 h at 823 K (550 °C) showing the spots compatible with the Fe_2SiTi phase in the following zone axes: (a) $\langle 100 \rangle$ axis, (b) $\langle 110 \rangle$ axis, and (c) $\langle 111 \rangle$ axis.

B. Transmission Electron Microscopy

We report here TEM observations after 3 hours of aging at 823 K (550 °C). Figure 2 shows the diffraction patterns recorded along three zone axes of the Fe matrix, namely, $\langle 100 \rangle$, $\langle 110 \rangle$, and $\langle 111 \rangle$. The first two zone axes show superstructure spots, whereas none is visible on the third zone axis. These diffraction patterns are compatible with the presence of the Heusler phase Fe_2SiTi .^[8] On dark-field micrographs, it was possible to identify spherical precipitates. However, due to the small precipitate size and sample oxidation, these observations were of poor quality and are not shown here.

C. Atom Probe Tomography

APT observations were carried out for different aging times at 823 K (550 °C), namely, 2, 3.5, 6, and 20 hours. The three-dimensional spatial distribution of solute atoms in these four samples is shown in Figure 3. Such images do not provide useful information on chemistry; however, they give a good visualization of the precipitate morphology and scale. In all cases, the microstructure consists of a relatively homogeneous distribution of

near-spherical precipitates, the size of which clearly increases with aging time. It also can be very clearly observed that the solute remaining in solid solution becomes scarcer when aging proceeds.

Precipitates were isolated from the matrix using isoconcentration surfaces. The interface between the matrix and each precipitate was chosen as the surface linking all the loci having a local concentration value of $(\text{Ti} + \text{Si}) = 25$ at. pct. The defined isosurfaces matched perfectly the precipitates observed in atom maps. For each of these aging conditions, solute profiles were drawn using the proxigram method.^[19] Concentrations are calculated at increasing distances from the previously defined isosurfaces, which are considered as the interface between the precipitate and matrix. The distances are positive on the precipitate side of the interface (within the particles) and negative on the matrix side. The resulting proxigrams (averaged on all precipitates obtained in the measured atom probe volume) are shown Figure 4 for the different aging times corresponding to Figure 3. In all cases, a diffuse compositional layer is found between the matrix and the precipitates. This diffuse interface extends over 1 nm on each side, partly due to the sampling lengths used in isosurface and proxigram calculations. Another

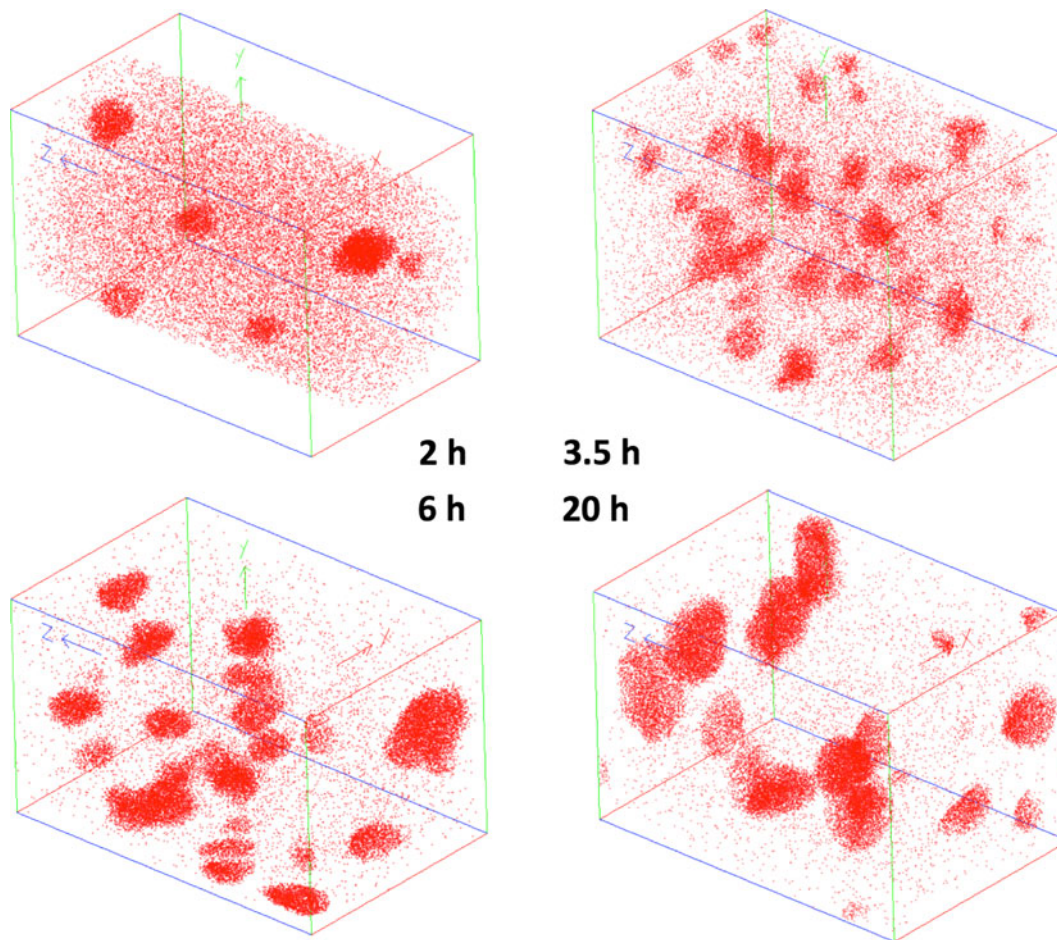


Fig. 3—APT reconstructions after 2, 3.5, 6, and 20 h at 823 K (550 °C). Fe atoms are not represented, and Si and Ti atoms are presented with a red color.

source of artificial interface spread could be due to differences in evaporation fields between the two phases (local magnification effect). As a consequence, at this stage, no information related to an actual composition gradient across the interfaces can be derived from the presented data. However, away from the interface, the proxigram shows a stable composition of the precipitate's core, with equal proportions of Ti and Si, and an Fe content between 50 and 60 at. pct. Each concentration value is obtained over more than 10,000 ions, making the standard deviation on each value smaller than 0.1 at. pct,^[20] so that statistical fluctuations are a negligible source of uncertainty. As the proxigrams were calculated over the full population of precipitates, the obtained values are averaged over all precipitates, which could hide important scatters around averaged values. The individual composition of each particle, therefore, was measured, and the result is presented in Figure 4(e) for the alloy aged 6 hours. No significant deviation from the average composition is observed. Therefore, it can be concluded that the analyzed samples contained a single population of precipitates, whose composition is fully compatible with the Heusler phase Fe₂SiTi. The slightly higher Fe content as compared to that of the Fe₂SiTi phase could be due to a small substitution of Fe to Si and Ti within the phase.

D. Small-Angle Neutron Scattering During Aging at 823 K (550 °C)

Figure 5 shows an example of a neutron scattering image obtained on a sample aged 3.5 hours at 823 K (550 °C). The anisotropic scattering contrast is clearly visible, as expected under a saturating magnetic field when precipitates are magnetic holes in a saturated ferritic matrix. Using an angular fit of the intensity such as done, *e.g.*, in Reference 21, it is possible to separate the magnetic and nuclear scattering intensities, which are shown for this particular example in Figure 5 in a Kratky plot $I\mathbf{q}^2$ vs \mathbf{q} (where I is the scattered intensity and \mathbf{q} the scattering vector) and in a Guinier plot of $\ln(I)$ vs \mathbf{q}^2 .

When the microstructure consists of a distribution of spherical precipitates, it was shown in Reference 22 that, provided that the width of the precipitate size distribution is in a reasonable range (relative standard deviation of about 20 pct), the measurement of the Guinier radius using a self-consistent iterative procedure leads to a very good approximation of the average precipitate radius. Thus, the following procedure for precipitate size measurement was used in the present study.

First, the pseudo-Guinier radius was measured from the scattering vector \mathbf{q}_{\max} , where $I\mathbf{q}^2$ shows a maximum value (maximum of the Kratky plot):

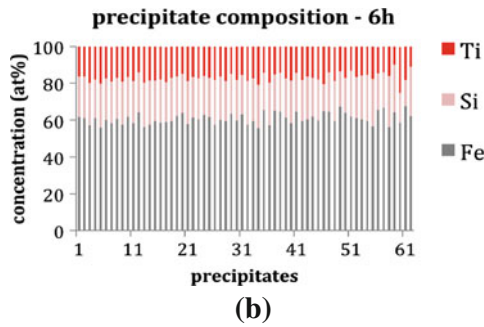
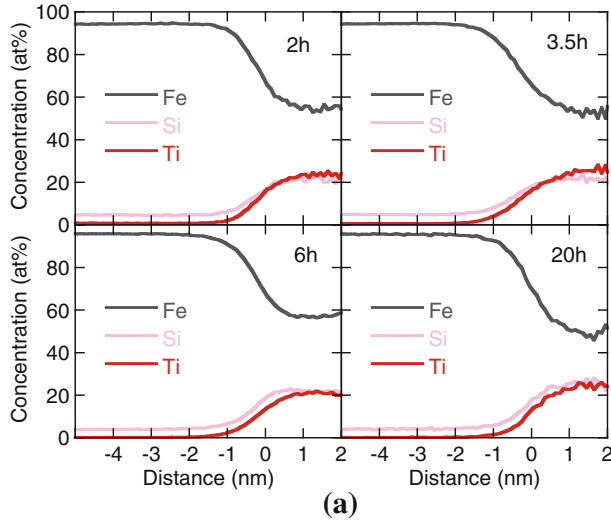


Fig. 4—(a) Concentration profiles from APT analysis across the matrix-precipitate interfaces after 2, 3.5, 6, and 20 h at 823 K (550 °C) and (b) measured concentrations for the sample aged 6 h for several precipitates.

$$R_g(1) = \frac{\sqrt{3}}{q_{\text{Max}}} \quad [1]$$

Then, the Guinier radius $R_g(I + 1)$ is determined by a linear fit to the Guinier plot $\ln(I)$ vs q^2 using the fit boundaries $[1.2/R_g(i), 2.8/R_g(i)]$ until convergence is obtained:

$$R_g(i + 1) = \sqrt{-3 \alpha} \quad [2]$$

where α is the slope of the Guinier plot. The precipitate radius is then taken equal to the final value of R_g :

$$R \cong R_g(n) \quad [3]$$

For the precipitate volume fraction, the integrated intensity Q_o is first calculated using the measured scattering intensity Q_o^{mes} :

$$Q_o^{\text{mes}} = \int_{q_1}^{q_2} I_{\text{cor}}(\mathbf{q}) q^2 d\mathbf{q} \quad [4]$$

where $I_{\text{cor}}(I) = I(\mathbf{q}) - I_{\text{const}}$, I_{const} being the constant intensity due to Laue scattering and incoherent scattering,

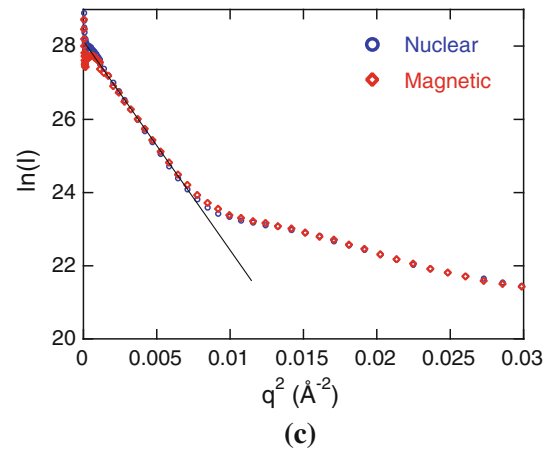
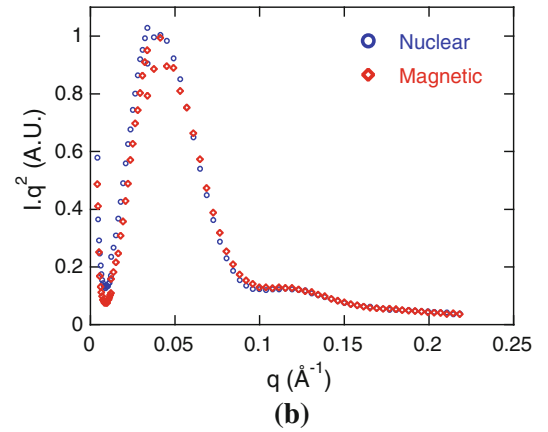
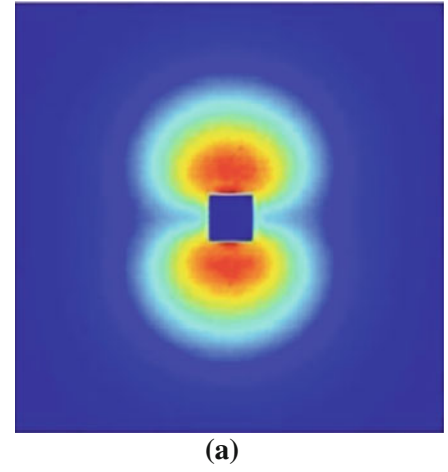


Fig. 5—(a) Example of SANS image for the sample aged 3.5 h at 823 K (550 °C). (b) Extracted nuclear and magnetic scattered intensities in a Kratky plot, normalized by the contrasts using the assumptions of magnetic hole for the magnetic intensity and of a precipitate composition of Fe_2SiTi for the nuclear intensity. (c) Same data in a Guinier representation.

measured using the asymptotic Porod behavior at large scattering vectors $I(\mathbf{q}) = K \cdot q^{-4}$. q_1 and q_2 are the boundaries of the measured range of scattering vectors. The total integrated intensity is then evaluated by using appropriate extrapolations outside the measured \mathbf{q} range (Reference 23 provides details):

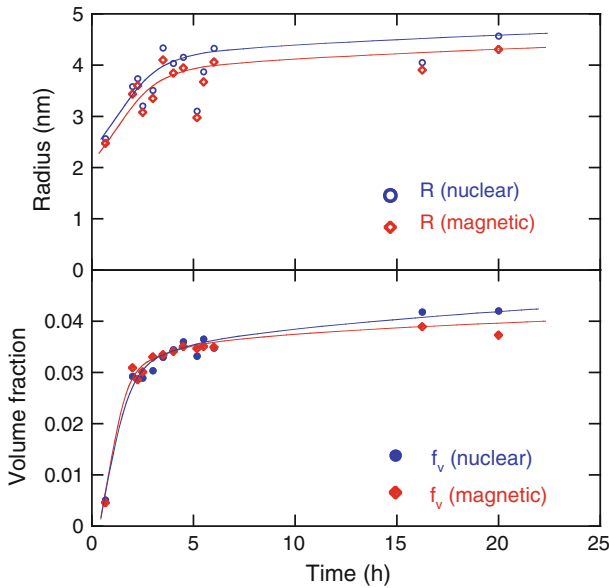


Fig. 6—Evolution of radius and volume fraction of precipitates with aging time at 823 K (550 °C) calculated from the nuclear and magnetic contributions of the scattered intensity.

$$Q_o = \frac{I_{\text{cor}}(\mathbf{q}_1) \mathbf{q}_1^3}{2} + Q_o^{\text{mes}} + \frac{K}{\mathbf{q}_2} \quad [5]$$

The volume fraction f_v is then simply calculated from the classical two-phase relationship:

$$Q_o = 2\pi^2 f_v (1 - f_v) \Delta\rho^2 \quad [6]$$

where $\Delta\rho$ is the contrast in neutron scattering length density between the precipitates and matrix:

$$\Delta\rho = \frac{b_p}{\Omega_p} - \frac{b_m}{\Omega_m} \quad [7]$$

where b_p and b_m are the average scattering length per atom in the precipitate and matrix, and $\Omega_p = 11.62 \text{ \AA}^3$ and $\Omega_m = 11.73 \text{ \AA}^3$ are the average atomic volumes in the precipitate and matrix. For the nuclear intensity, $b_{\text{Ti}} = -3.438 \times 10^{-5} \text{ \AA}$, $b_{\text{Si}} = 4.1491 \times 10^{-5} \text{ \AA}$, and $b_{\text{Fe}} = 9.45 \times 10^{-5} \text{ \AA}$. The matrix nuclear scattering length is approximated from the initial alloy composition, and the precipitate nuclear scattering length is calculated assuming a composition of Fe_2SiTi :

$$b_m^{\text{nucl}} = 9.31 \times 10^{-5} \text{ \AA} \quad \text{and} \quad b_p^{\text{nucl}} = 4.90 \times 10^{-5} \text{ \AA}$$

For the magnetic contrast, precipitates are considered to be magnetic holes so that

$$b_m^{\text{mag}} = 5.98 \times 10^{-5} \text{ \AA} \quad \text{and} \quad b_p^{\text{mag}} = 0$$

Figure 6 shows the evolution of precipitate size and volume fraction, measured both from the nuclear and magnetic scattering curves for different aging times at 823 K (550 °C). These curves show that the data

obtained from the two contributions are always very consistent. This further validates the hypotheses made for the volume fraction calculations, namely, a precipitate composition of Fe_2SiTi for the nuclear contribution and nonmagnetic precipitates for the magnetic contribution.

The initial precipitate radius is of the order of 2.5 nm. It corresponds to a very low volume fraction and, therefore, is probably close to the nucleation radius. Then the precipitate radius rapidly increases to about 4 nm and stabilizes. The volume fraction is observed to increase rapidly as well, almost reaching the saturation value of 4 pct after 2 hours of aging.

Some variations on the precipitate radius are observed along the aging curve. However, after having repeated some experiments, we do not believe that these variations have a physical meaning. They are probably due to some variability of the process from sample to sample, such as in the alloy chemistry or some steps of the heat treatment.

E. Effect of Aging Procedure on Precipitation at 823 K (550 °C)

In order to check if the details of the temperature history during the initial stages of precipitation have an influence on the precipitation kinetics, several thermal paths were applied for the 823 K (550 °C) aging treatment (Section II-A), where the temperature path from the solution treatment temperature to the aging temperature was either monotonously decreasing (transfer from the 1173 K (900 °C) salt bath to the aging salt bath) or interrupted by quenching to room temperature and reheating. Possible effects of early stage temperature history could include changes in vacancy concentrations or changes in the precipitate nucleation rate and, thus, precipitate number density.

Figure 7 shows the evolution of precipitate radius and volume fraction along the 823 K (550 °C) heat treatment. The influence of the aging procedure on the precipitation kinetics appears to be very limited, both in terms of radius and volume fraction. The results of the different thermal paths cannot be discriminated within experimental uncertainty.

F. Effect of Temperature on Precipitation Kinetics

Last, the influence of temperature on the precipitation kinetics was investigated in the range 723 K to 853 K (450 °C to 580 °C). For all temperatures tested, except 823 K (550 °C), as reported previously, only SANS experiments were performed, preventing any direct evidence of the nature of precipitates that form. However, at 823 K (550 °C), the dominant phase was the metastable Fe_2SiTi phase, which is coherent with the Fe matrix. At temperatures lower than 823 K (550 °C), it is likely that the same coherent metastable phase will have an even stronger tendency to form. It is assumed that this is also the case at 853 K (580 °C), a temperature close to 823 K (550 °C). The comparison between the nuclear and magnetic scattering intensities in the entire temperature range is actually consistent with this hypothesis.

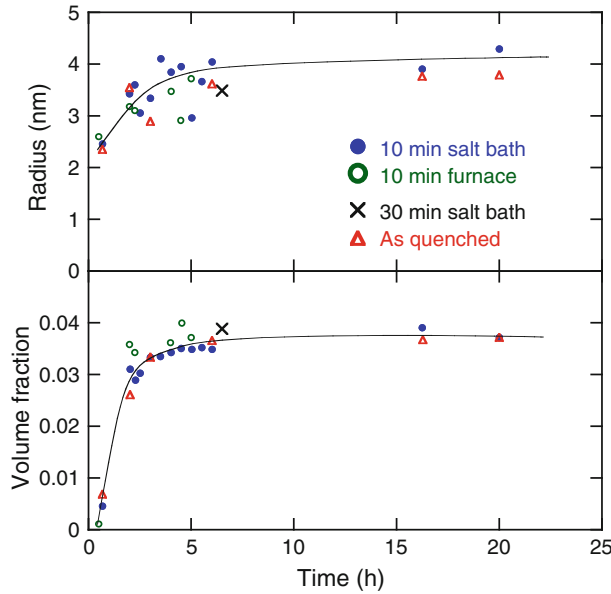


Fig. 7—Influence of the aging procedure on the evolution of precipitate size and volume fraction with aging time at 823 K (550 °C).

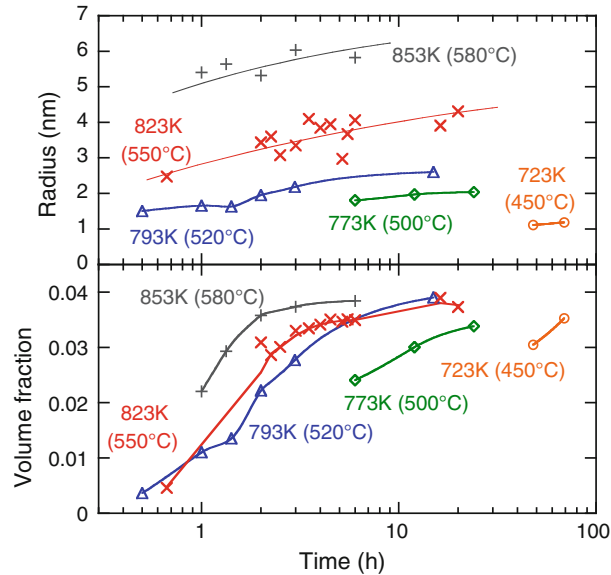


Fig. 8—Influence of temperature on the evolution of precipitate size and volume fraction with aging time.

Figure 8 shows the evolution of precipitate radius and volume fraction for the different aging times and temperatures investigated. As expected, the precipitate radius increases with temperature at a given aging time. The time ranges investigated are too limited to draw a conclusion about the influence of temperature on nucleation radius. The evolution of volume fraction is faster as temperature increases, showing that all the chosen temperatures are below the nose of the C curve for precipitation kinetics. It is expected that the equilibrium volume fraction would increase with decreasing temperature. Although the investigated time ranges do not enable direct illustration of this tendency, it seems to

be confirmed by the fact that the lower temperatures show a positive slope of volume fraction evolution at values close to the saturating volume fraction of higher temperatures.

IV. MODELING OF PRECIPITATION KINETICS

An overview of the precipitation model that was used to describe the experimental data follows. A class modeling approach was used, as described numerous times in the literature.^[24–26] In this model, the precipitate size distribution is discretized into classes of age. Each class of age evolves with time according to a growth/dissolution law that only depends on the solid solution concentration of the matrix; *i.e.*, no spatial interaction between neighboring precipitates is considered. Nucleation of new (young) particles introduces new classes in the distribution. In the present case, we have used a model implementation of the “Lagrangian” type such as described in Reference 27; namely the different size classes do not have a constant size: during the microstructural evolution the size of the classes evolves by growth or dissolution. Specific algorithms were developed to adjust the number of precipitate classes when they became too numerous (such as during nucleation) or too scarce (such as during coarsening).

The solubility of Si and Ti in the Fe matrix with respect to the Fe₂SiTi phase is described by a thermally activated solubility product:

$$\left(X_{\text{eq}}^{\text{Si}} X_{\text{eq}}^{\text{Ti}} \right)^{1/4} = K_{\text{eq}}(T) \quad [8]$$

where $X_{\text{eq}}^{\text{Si}}$ and $X_{\text{eq}}^{\text{Ti}}$ are the atomic fractions of Si and Ti at equilibrium.

The classical nucleation theory is used to assess the nucleation rate J of new particles:

$$J = \frac{Z\beta^*}{\Omega_p} \exp\left(-\frac{\Delta G^*}{k_B T}\right) \left(1 - \exp\left(-\frac{t}{\tau}\right)\right) \quad [9]$$

where Ω_p is the average atomic volume in the precipitate and Z is the Zeldovich factor:

$$Z = \frac{\Omega_p}{2\pi R^{*2}} \sqrt{\frac{\gamma}{k_B T}} \quad [10]$$

γ is the interfacial energy between the precipitates and the matrix, and R^* is the critical radius defined by

$$R^* = -\frac{R_o}{S} \quad [11]$$

where R_o is the capillarity radius:

$$R_o = \frac{2\gamma\Omega_p}{k_B T} \quad [12]$$

and S the supersaturation:

$$S = \ln\left(\frac{K_s}{K_{\text{eq}}}\right), \quad \text{where } K_s = \left(X^{\text{Si}} X^{\text{Ti}}\right)^{1/4} \quad [13]$$

X^{Si} and X^{Ti} are the atomic fractions in the ferrite solid solution of Si and Ti. β^* is the critical attachment rate that we calculate as the geometrical average (weighted by the precipitate compositions) of the attachment rates for Si and Ti:

$$\beta^* = \frac{4\pi R^{*2}}{a^4} \frac{1}{\frac{0.25}{D_{\text{Si}} X^{\text{Si}}} + \frac{0.25}{D_{\text{Ti}} X^{\text{Ti}}}} \quad [14]$$

where D_{Si} and D_{Ti} are the diffusion coefficients for Si and Ti and a is the lattice parameter of ferrite. ΔG^* is the activation barrier that is simply given by

$$\Delta G^* = \frac{4\pi R_o^2 \gamma}{3 S^2} \quad [15]$$

and τ is the incubation time defined by

$$\tau = \frac{2}{\pi \beta^* Z^2} \quad [16]$$

New particles are brought in the precipitate size distribution at a size R_{eff}^* slightly larger than the critical radius, so as to allow for subsequent growth:

$$R_{\text{eff}}^* = R^* + \frac{1}{2} \sqrt{\frac{k_B T}{\pi \gamma}} \quad [17]$$

After it has nucleated, a precipitate grows or shrinks following the classical Zener law that can be applied either on Si or Ti:

$$\frac{dR}{dt} = \frac{D_{\text{Si}} X_p^{\text{Si}} - X_i^{\text{Si}}}{R X_p^{\text{Si}} - X_i^{\text{Si}}} = \frac{D_{\text{Ti}} X_p^{\text{Ti}} - X_i^{\text{Ti}}}{R X_p^{\text{Ti}} - X_i^{\text{Ti}}} \quad [18]$$

where X_i^{Si} and X_i^{Ti} are the atomic solute fractions of Si and Ti in equilibrium with the precipitates of size R (that are considered equal to the interfacial atomic fractions under the hypothesis of local equilibrium). These concentrations are calculated by equating the two growth rates in Eq. [18] and using the Gibbs–Thomson modified solubility product:

$$(X_i^{\text{Si}} X_i^{\text{Ti}})^{1/4} = K_{\text{eq}} \exp\left(\frac{2\gamma \Omega_p}{R k_B T}\right) \quad [19]$$

The evolution of volume fraction and solute concentration is then simply calculated by integrating the precipitate size distribution and using a mass balance between the precipitates and matrix.

For the model adjustment to the experimental data, the diffusion coefficients for Si and Ti were taken from

the literature,^[28,29] and the values are reported in Table II. The only adjustable parameters left at a given temperature, therefore, were the value of the solubility product $K_{\text{eq}}(T)$ and of the precipitate interfacial energy γ . We chose to keep this last parameter constant as a function of temperature, as it is expected that in the investigated temperature range the change in interfacial energy would remain small. The model presented here assumes a homogeneous nucleation mechanism for the precipitates within the classical nucleation theory framework; therefore, no adjustable parameter related to nucleation was needed.

Figure 9 shows the comparison between the experimental results and the model (Table II shows the model parameters). The diffusion coefficients for Si and Ti were taken from the literature,^[28,29] the interfacial energy between the precipitates and the matrix was taken constant with temperature using a relatively low value of

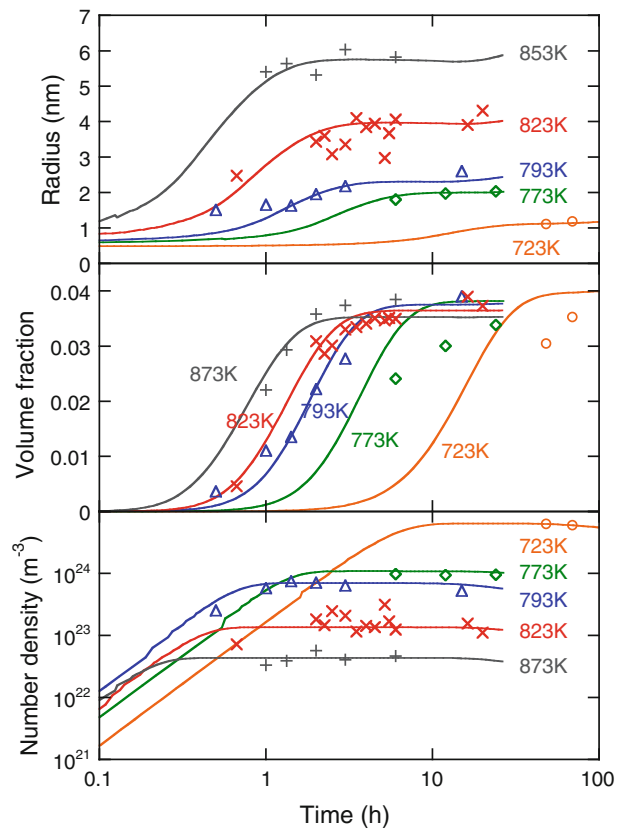


Fig. 9—Comparison between the experimental results and the results of the precipitation kinetics model for the different aging temperatures, in terms of precipitate size, volume fraction, and number density.

Table II. Parameters for the Precipitation Model

Parameter	Interfacial Energy γ	Diffusion Si		Diffusion Ti		Solubility Product	
		D_o^{Si}	Q^{Si}	D_o^{Ti}	Q^{Ti}	A	B
Unit	J m ⁻²	m ² s ⁻¹	kJ mol ⁻¹	m ² s ⁻¹	kJ mol ⁻¹	—	J
Value	0.13	9.2×10^{-5}	200.88	3.15×10^{-4}	248	0.716	2.27×10^{-20}

interfacial energy of 0.13 J m^{-2} , which is reasonable given the coherent nature of the interface and the high Fe content in the precipitates. The solubility product was adjusted at each temperature. Figure 10 shows an Arrhenius plot of its evolution with temperature. The evolution is approximately linear, so that a solubility product $K_{\text{eq}} = A \exp(-B/k_B T)$ (compositions in atomic fractions) provides a good description of all our experimental data, with $A = 0.716$ and $B = 2.27 \times 10^{-20} \text{ J}$. The agreement is good at all temperatures, especially given the fact that the nucleation was described by a simple classical nucleation theory, which provides in many systems an insufficient nucleation rate.

Now that the model is validated over a range of temperatures on the investigated alloy, it can be tentatively applied to other compositions. Particularly, it is interesting to evaluate the possible influence of the Si:Ti ratio on the precipitation kinetics. The studied alloy has a significant excess of silicon, and titanium diffuses slower and, therefore, should control the precipitate growth kinetics. The model was run on different compositions (Table III), which have the same value of the initial solubility product $X_{\text{Si}} X_{\text{Ti}}$, so that the initial alloy supersaturation is the same for all alloys.

Figure 11 shows the different precipitation kinetics predicted by the model, assuming that the same phase, Fe_2SiTi , is forming in all alloys. We find a relatively small influence of the Si/Ti ratio on the evolution of

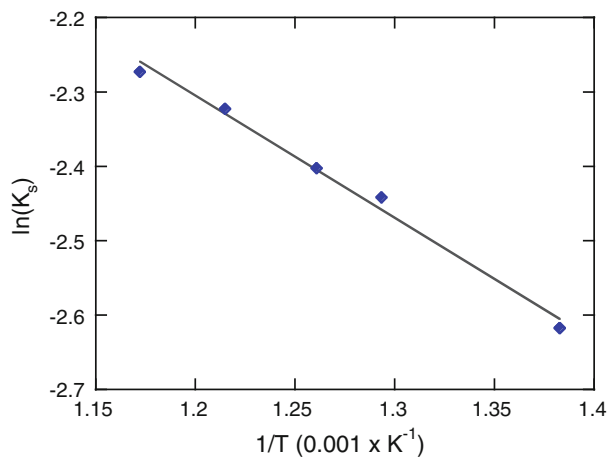


Fig. 10—Evolution of the solubility product K_s determined to obtain the model results shown in Fig. 9 as a function of temperature.

precipitate sizes. Only the alloy containing more titanium than silicon is predicted to have a markedly different evolution of radius with time. This lack of influence could be due to the fact that titanium is the diffusion-controlling element and, thus, controls the kinetics. However, an important increase in volume fraction with increasing titanium content is observed. This is consistent with the experimental observations made by Abson *et al.*^[5] and with the fact that, except for alloy 5, all other alloys have excess Si. Logically, the maximum volume fraction is obtained for a Si:Ti ratio close to 1.

This parametric study shows that maximizing the strengthening potential of these precipitation hardening alloys requires approaching the Si:Ti stoichiometry line, since the volume fraction can be substantially increased without much detrimental effect of the precipitate size. Of course, this does not include more complex effects, such as a possible change of precipitate type with alloy composition or the effect of solid solution on the plasticity behavior of the alloy (especially silicon).

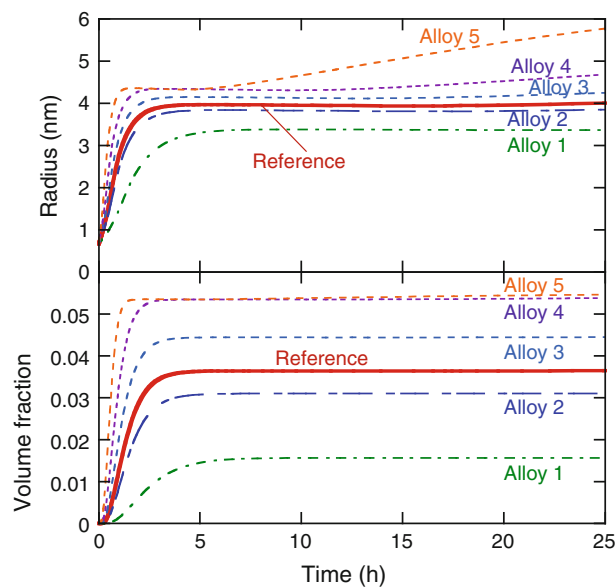


Fig. 11—Effect of the Si:Ti ratio (corresponding alloy compositions are given in Table II) on the evolution of precipitate size and volume fraction predicted by the model during aging at 823 K (550 °C).

Table III. Composition of Alloys Used for Modeling the Influence of Alloy Composition on the Ageing Kinetics; the Reference Alloy is the Alloy Used for the Experimental Investigation

Alloy	1	2	Reference	3	4	5
Si (at. fraction)	0.117	0.059	0.0492	0.039	0.029	0.02
Ti (at. fraction)	0.005	0.01	0.0119	0.015	0.02	0.029
Si/Ti	23.4	5.8	4.1	2.6	1.5	0.7

V. CONCLUSIONS

We have carried out a systematic study of precipitation kinetics in a Fe-Si-Ti alloy for a range of aging times and temperatures, combining complementary tools (TEM, APT, and SANS). Our results show that in the temperature range 723 K to 823 K (450 °C to 550 °C), precipitation was dominated by the Heusler phase Fe₂SiTi, whose stoichiometry was slightly enriched in Fe. The precipitation kinetics obeys a classical behavior as a function of time and temperature and has been shown to be independent of the details of the initial temperature history (such as a direct aging at the aging temperature or a reheating from room temperature). Numerical models based on the evolution of precipitate size classes were shown to be in very good agreement with the experimental results, using a simple hypothesis such as thermodynamics described by a solubility product, a classical nucleation theory approach, and a Gibbs–Thomson corrected Zener growth rate for individual size classes. The application of the model to different alloy compositions was also investigated and was shown to provide potential directions for alloy optimization.

ACKNOWLEDGMENTS

The authors acknowledge Dr. C. Dewhurst and the ILL staff for the technical help during the SANS experiments at the Institut Laue Langevin (Grenoble, France). Thanks is extended to The ArcelorMittal Research MPM team for help with the preparation and transformation of the FeSiTi sheets. Dr. D. Mangelinck is gratefully thanked for his support and fruitful discussions.

REFERENCES

1. R. Wasmuht: *Arch. Eisenhüttenwes*, 1931, vol. 5, p. 45.
2. R. Vogel: *Arch. Eisenhüttenwes*, 1938, vol. 12, pp. 207–12.

3. J.P. Henon, J. Manenc, and C. Crussard: *C.R. Acad. Sci.*, 1963, vol. 257, p. 671.
4. J.P. Henon, C. Waché, and J. Manenc: *Mem. Sci. Rev. Metall.*, 1966, vol. LXIII.
5. D.J. Abson, G.G. Brown, and J.A. Whiteman: *J. Aus. Inst. Met.*, 1968, vol. 13.
6. T. Bracewell: *Low Alloy Steels*, Conf. Proc. Iron and Steel Institute in London, 1968, pp. 229–39.
7. R. Papaleo and J.A. Whiteman: *Micron*, 1971, vol. 2, pp. 63–70.
8. D.H. Jack: *Met. Sci. J.*, 1970, vol. 4.
9. D.H. Jack and W.K. Honeycombe: *Acta Metall.*, 1972, vol. 20, pp. 787–96.
10. D.H. Jack and F. Guiu: *J. Mater. Sci.*, 1975, vol. 10, pp. 1161–68.
11. D.M. Schwartz and B. Ralph: *Met. Sci. J.*, 1969, vol. 3, pp. 216–19.
12. V. Raghavan: *Phase Diagrams of Ternary Iron Alloys, Part 1*, ASM INTERNATIONAL, Metals Park, OH, 1987, pp. 65–72.
13. V. Raghavan: *J. Phase Equilib. Diffus.*, 2009, vol. 30, pp. 393–96.
14. W. Xiong, Y. Du, and C. Zhang: *Iron Systems: Phase Diagrams, Crystallographic and Thermodynamic Data*, Landolt-Börnstein New Series, 2009, p. IV/11 D5.
15. F. Löffler, M. Palm, and G. Sauthoff: *Steel Res. Int.*, 2004, vol. 75, pp. 766–72.
16. F. Weitzer, J.C. Schuster, M. Naka, F. Stein, and M. Palm: *Intermetallics*, 2008, vol. 16, pp. 273–82.
17. H. Leitner, M. Bischof, H. Clemens, S. Erlach, B. Sonderegger E. Kozeschnik, J. Svoboda, and F.D. Fischer: *Adv. Eng. Mater.*, 2006, vol. 8, pp. 1066–77.
18. M.K. Miller and G.D.W. Smith: *Atom Probe Microanalysis: Principles and Applications to Material Problems*, Materials Research Society, Pittsburgh, PA, 1989.
19. O.C. Hellman, J.A. Vandenbroucke, J. Rusing, D. Isheim, and D.N. Seidman: *Microsc. Microanal.*, 2000, vol. 6, pp. 437–44.
20. F. Danoix, G. Grancher, A. Bostel, and D. Blavette: *Ultramicroscopy*, 2007, vol. 107, pp. 739–43.
21. F. Perrard, A. Deschamps, F. Bley, P. Donnadieu, and P. Maugis: *J. Appl. Crystallogr.*, 2006, vol. 39, pp. 473–82.
22. Alexis. Deschamps and Frédéric. De Geuser: *J. Appl. Crystallogr.*, 2011, vol. 44, pp. 343–52.
23. F. De Geuser and A. Deschamps: *C.R. Phys.*, 2012, vol. 13, pp. 246–56.
24. J.D. Robson, M.J. Jones, and P.B. Prangnell: *Acta Mater.*, 2003, vol. 51, pp. 1453–68.
25. O.R. Myhr and O. Grong: *Acta Mater.*, 2000, vol. 48, pp. 1605–15.
26. M. Nicolas and A. Deschamps: *Acta Mater.*, 2003, vol. 51, pp. 6077–94.
27. M. Perez, M. Dumont, and D. Acevedoreyes: *Acta Mater.*, 2008, vol. 56, pp. 2119–32.
28. W. Batz, H.W. Mean, and C.E. Birchenal: *Trans. AIME*, 1953, p. 1170.
29. T. Gladman: *The Physical Metallurgy of Microalloyed Steels*, Asgate Publishing, 1997.